Inconsistent responses of cells on operating conditions in a 5 kW proton exchange membrane fuel cell stack

Xuexia Zhang , Yu Jiang , Lei Huang , Weirong Chen , Dan Brett

PII: S0013-4686(21)01215-9
DOI: https://doi.org/10.1016/j.electacta.2021.138925
Reference: EA 138925

To appear in: *Electrochimica Acta*

Received date: 14 December 2020
Revised date: 30 June 2021
Accepted date: 12 July 2021

Please cite this article as: Xuexia Zhang , Yu Jiang , Lei Huang , Weirong Chen , Dan Brett , Inconsistent responses of cells on operating conditions in a 5 kW proton exchange membrane fuel cell stack, *Electrochimica Acta* (2021), doi: https://doi.org/10.1016/j.electacta.2021.138925

Inconsistent responses of cells on operating conditions in a 5 kW proton exchange membrane fuel cell stack

Xuexia Zhang [a, b, *], Yu Jiang [a], Lei Huang [a], Weirong Chen [a, b], Dan Brett [c]

[a] School of Electrical Engineering, Southwest Jiaotong University, Chengdu, 611756, China

[b] National Rail Transportation Electrification and Automation Engineering Technology Research Center, Southwest Jiaotong University, Chengdu, 611756, China

[c] Department of Chemical Engineering, University College London, WC1E 6BT, UK

* Corresponding author. *E-mail address*: survival_zxx@sina.com (X. X. Zhang); Tel.:+8613908227317 (X. X. Zhang)

Abstract: The cell inconsistency investigation for large-scale proton exchange membrane fuel cell (PEMFC) stacks is significant. In this paper, the inconsistency between fault cells and normal ones is investigated in a 5 kW stack with 30 cells of the active area of 312 cm^2. Considering typical operating conditions, the stack temperature and hydrogen/air stoichiometry are investigated to discuss the effects on the inconsistency. As comprehensive indexes, voltage performance, polarization curve, and electrochemical impedance spectrum (EIS) are presented to evaluate the above experiments. To enhance the EIS resolution, the distribution of relaxation times (DRT) is applied to extract the characteristic frequency points from the EIS ranged from 0.5 Hz to 10 kHz. In conclusion, fault cells are sensitive to operating conditions with poor performance and larger polarization resistance compared with the normal cells. Furthermore,

the DRT can well quantify the inconsistency of impedances produced by oxygen diffusion (fault 0.5 ~ 4.0 mΩ and normal 0.3 ~ 1.0 mΩ) and oxygen reduction reaction (fault 0.7 ~ 1.5 mΩ and normal 0.5 ~ 0.6 mΩ), respectively. Meanwhile, the inconsistency strongly relates to the operating conditions. Moreover, the damaged structure of fault cells in membrane electrode assemblies further validates the inconsistency by scanning electron microscopy.

Keywords: Proton exchange membrane fuel cell stack; Cell inconsistency; Electrochemical impedance spectrum; Scanning electron microscopy; Distribution of relaxation times

1. Introduction

Proton exchange membrane fuel cell (PEMFC) is an attractive energy option with its advantages of zero pollution, low running temperature, and high conversion efficiency. Its scale and power class are greatly promoted due to the energy policies and commercialization worldwide. In industrial fields, the large-scale PEMFC stacks are a promising application of vehicles, trams and locomotives [1–7]. However, the fault cells that appeared in the operation process, ordinarily, determine the stack performance and lifetime. Therefore, how to accurately identify and locate the fault cells and investigate the inconsistent responses in large-scale stacks are of essentiality to improve the property and durability [8].

A single cell or a small-scale stack is the objective of most available studies which focus on fault diagnosis and cell inconsistency. Mohammadi et al. [9] applied a single cell to conduct a novel diagnosis method for flooding and drying based on temperature and current density distribution. As for the diagnosis via impedance methods, the cells with a small-scale active area are most in consideration due to their stability and homogeneity during tests [10–13]. Roy and Orazem [13] applied a cell with a 5 cm^2 active area to detect the onset of flooding using impedance techniques. Fouquet et al. [12] measured the impedance spectrum of a six-cell stack to evaluate the cell state of health (SoH) based on their proposed equivalent circuit model. When concerning cell inconsistency, a four-cell stack [14], a five-cell stack [15], and a customized stack [16] are applied in their studies, respectively. Hu et al. [14] studied the inconsistency of different parts in a single cell under varying load. Lin et al. [15] analyzed the cell inconsistency under cold start-up and found the middle cell performed better than the bilateral ones while the cell degradation intensified from inlet to outlet. Moreover, the inconsistency

phenomenon in a four-cell stack was investigated at the SoH of flooding, drying, and hydrogen starvation [16]. Inconsistency analysis on a small-scale stack is of significance to explore the propagative and evolutionary mechanisms among single cells inside. Nevertheless, what is noteworthy is that the direct extension of the conclusions on fault diagnosis and cell inconsistency from a small-scale stack to a large-scale stack is not solid enough in theory and experiment, since the differences of size and number bring about the difficulties of species transport, heterogeneities of physical-field distribution and component materials distribution, and the complexities of cell interactions. Therefore, it is necessary to further investigate the large-scale stacks and explore the relationships of single cells inside.

With the commercial promotion and application of PEMFC-based vehicles, trams and locomotives, the studies paying attention to kW-class even larger stacks or multi-stacks are as much as popular recently. Hence, it is important, as far as possible, to maintain the stack performance and prolong the remaining useful lifetime [17], [18] due to the various stochastic processes in practice, which are detrimental to the cell components and materials. The fault diagnosis at water management issues at the stack level, to the knowledge of the authors, is a common method up to now [19–22]. Ifrek et al. [23] measured a 100-cell stack and concluded that flooding and drying can be detected via current distribution. Debenjak et al. [24] successfully detected flooding and drying inside an 80-cell PEMFC stack. Moreover, the system faults regarding air supply were diagnosed conducted by a 40-cell stack through the stack voltage signal [19] and the magnetic data [20], respectively. Except for the studies on fault diagnosis, Chen et al. [25] investigated the intake inconsistency using two side-by-side placed 40 kW stacks sharing one feeding system; this study mainly concerns the difference of reactant supply between stacks while not the cell inconsistent performance inside. In practical industries, system

reliability of the multi-stacks or stack is principally affected by the poor ones or cells generally. If the existence of this inconsistency is chronically neglected during the operation, in addition to the performance loss, it will lead to serious security issues to the overall system. Therefore, during the long-term running, it is not only to conduct fault diagnosis for the stack but also to pay attention to the internal cell inconsistency timely. However, it should be noted that only a few available studies have focused on cell inconsistency in the large-scale PEMFC stacks. Li et al [26] investigated the cell non-uniformity, based on the voltage responses, in a 14.4 kW PEMFC stack under dynamic load changes and condition variations. This paper, in the following sections, will comprehensively discuss the cell inconsistency in a 5 kW stack from voltage response, impedance spectroscopy, and component structure.

In regard to the measurements to PEMFCs, voltage monitoring, electrochemical impedance spectroscopy (EIS) tests and visualization techniques are the most frequent types. Voltage monitoring is to detect the voltage responses, for instance, polarization curve, static performance, and dynamic behavior [27–29] for both single cells and the stack in real-time [14], [30]. A two-point voltage monitoring experiment was conducted in a customized PEMFC stack [14], [15] to study the cell inconsistent responses. The results indicated that this novel approach shows precision in locating fault cells. The voltage responses in the stacks are monitored in real-time and an inconsistency index is applied to represent the cell non-uniformity under dynamic load changes [26], [31]. The polarization curves are used to analyze the electrochemical features [32] and to predict the performance [33] of PEMFC. Moreover, the static performance is used to analyze the effects of parameter changes including cell components [34] and operating conditions [28], [35] on the PEMFC. As for voltage monitoring, it is a very convenient and inexpensive tool of performance characterization and fault

diagnosis for the single cells or the stack. However, it exhibits some deficiencies, as well, in describing the complicated reaction processes inside PEMFC.

The EIS test is to obtain the impedance data, such as ohmic resistance and polarization resistance, represented in the frequency domain by calculating voltage responses at the superimposed alternating current [12], [36]. The exploration of internal processes, the assistance of the mechanism studies, and the fault diagnosis via the spectra changes are some of the purposes of applying the EIS techniques for PEMFCs [11,37–40]. Yuan et al. [37] measured the EIS to well clarify the internal polarization process for the PEMFC. Heinzmann et al. [38] investigated the changes of the reaction processes inside by testing the cell EIS under various current densities. Voigts et al. [41] identified the electrode reaction mechanisms of the solid oxide fuel cell by deconvoluting its measured EIS. Araya et al. [42] applied the EIS technique to a commercial stack to investigate the fault characterization. Another impedance-based method is the distribution relaxation of times (DRT), which is calculated from the complex impedance data and assistants to study some processes that are inconspicuous in the impedance spectra. The contribution of anode and cathode processes to impedance was investigated in [38] by DRT analysis through hydrogen/air and hydrogen/hydrogen tests. Similarly, the DRT plots are used in [37] to analyze the varying trend of the transport process in PEMFC at different MEA humidity, oxygen diffusion coefficient, and membrane thickness. On the other hand, the DRT can also help to identify the cell impedance spectrum and to select suitable initial values of the equivalent circuit model [43]. The advantages of EIS and DRT are very fascinating in PEMFC researches, however, the time-consuming impedance tests make it difficult to be achieved in online diagnosis. Regarding this stack, the authors mainly focus on the inconsistency of reaction processes in different cells while not the diagnosis in real-time, hence its deficiency in time domain is not discussed in this paper.

The visualization technologies are the most direct characterization means to observe the PEMFC, which can be used to visualize the internal structure and to identify the failed components. The technologies of scanning electron microscopy (SEM), neutron radiography, and X-ray imaging applied to PEMFC studies have been reported in recent decades [44], [45]. Wang et al. [46] employed the SEM to observe membrane electrode assemblies (MEAs) and found that dynamic load cycles severely accelerate catalyst degrading. Farmer et al. [47] studied the gas diffusion layer (GDL) porosity using SEM imaging and the results well conformed to the mercury intrusion porosimetry. Lochner et al. [48] visualized an end-of-test MEA which experienced a realistic running and the results demonstrated that local regions suffered different levels of degradation. Aoyama et al. [44] reported a visualization of the water transport process in the microporous layer of PEMFC by cryo-SEM technique. It is generally to conduct SEM test at the end of PEMFC running since it is an *ex-situ* characterization tool and destructive to the MEA. Therefore, the selected cells in this paper are conducted SEM analysis after the stack operated for a long term.

This work is conducted to have a better understanding and to explain the inconsistency characterization among the cells in a large-scale PEMFC stack, which operates under the same conditions. In this paper, a comprehensive analysis including voltage response, EIS and DRT plots, and SEM imaging is conducted to a 30-cell PEMFC stack to evaluate the cell inconsistency inside. Thereinto, the voltage responses of single cells are used to analyze the non-uniform performance inside this stack as well as locate the fault cells during the long-term operation. In order to analyze the inconsistency of mechanisms and reaction processes, several cells including the normal and the faulty are selected according to the voltage responses. The transport resistance of each selected cell is analyzed and compared through its EIS plots under various operating conditions. Moreover, the

corresponding DRT plots are applied to assess and compare two primary processes, one is oxygen diffusion and another is the oxygen reduction reaction. When this stack achieves the end of tests, the MEAs of two different cells are conducted SEM visualization to observe their inconsistent structure and analyze the degradation or damage extent.

The framework of this paper layouts as follows. Experimental devices, testing procedures, and the mathematical theories of the validation of EIS tests and the DRT method are presented in Section 2. The inconsistency analysis between cells under various operating conditions of temperature and reactant supply is discussed in Section 3. At last, this paper is concluded in Section 4.

2. Experimental

2.1 Experimental devices and measurements

In this study, a 30-cell PEMFC stack typed HySTK-5 (Sunrise Power Co. Ltd) with a single-cell MEA active area of 312 cm^2 is measured. The experiments are conducted using a 15 kW test bench typed RG-FCTS-15 (W-RIG Co., Ltd), which can regulate the operating conditions and record input/output parameters instantaneously. The impedance measurements are carried out using a multi-channel test station model TrueData EIS (FuelCon AG Inc.) under the stack operated in the ohmic loss region. The schematic of the above devices is illustrated in Fig. 1a.

In this study, three types of measurements are conducted under the operating conditions of:

(i) stack temperature (T_{ST}) from 35 °C to 70 °C

(ii) anode hydrogen stoichiometric (S_A) from 2.0 to 1.1

(iii) cathode air stoichiometric (S_C) from 3.0 to 1.7

where the experimental tests including polarization curves and impedance measurements are carried

out in galvanostatic mode with the electric load uploading commanded current from 0 to 160 A, and constant current 100 A, respectively. In addition to the above mentions (i) ~ (iii), the other parameters remain of anode gauge pressure at 0.85 bar and cathode gauge pressure at 0.7 bar. Moreover, the relative humidity (R.H.) of hydrogen is ambient humidity while the air well humidified (100% R.H.). The voltage data of cells and the stack is recorded by the test bench every 0.5 seconds.

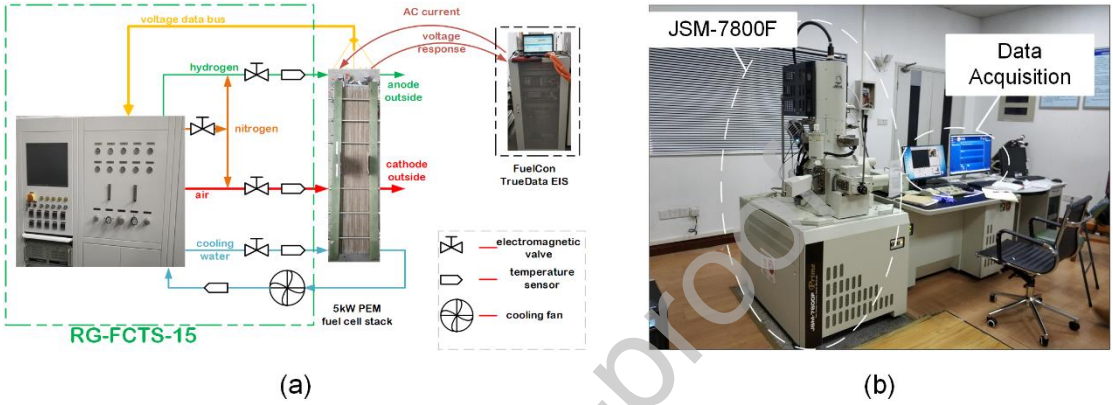

Fig. 1 The experimental devices for the measurements of (a) Performance test system including voltage monitoring and EIS test by RG-FCTS-15 and TrueData EIS, and (b) MEA detection by JSM-7800F.

Individually, the stack temperature and gas flow rates are regulated to satisfy the measurement requirements abovementioned. Each state was operated last 15 minutes to conduct EIS measurements for five selected cells. The current amplitude of 10 A is superimposed to obtain the spectra in the frequency range from 10 kHz to 0.5 Hz with 16 recorded points. After all tests, the MEAs are observed and analyzed for a comparative study using a field emission scanning electron microscope modeled JSM-7800F, which is shown in Fig. 1b.

2.2 Kramers-Kronig validity test

Favorable data quality and high signal-to-noise ratio are serious for impedance acquisition since the electrochemical processes can be disturbed by even a small noise. Therefore, validity verification is required for the measured data set before applying the DRT. A general method for validation is Kramers-Kronig (K-K) transform for impedance data [49]. As the data satisfies the causality, linearity

and stability, the real and imaginary parts follow the relations:

$$\mathrm{ReZ}(\omega)=\frac{2}{\pi}\int_0^{\infty}\frac{\omega'\mathrm{ImZ}(\omega)}{\omega^2-\omega'^2}\mathrm{d}\omega' \qquad \mathrm{ImZ}(\omega)=-\frac{2}{\pi}\int_0^{\infty}\frac{\omega\mathrm{ReZ}(\omega)}{\omega^2-\omega'^2}\mathrm{d}\omega' \tag{1}$$

where $\mathrm{ReZ}(\omega)$ represents the real part of the impedance, $\mathrm{ImZ}(\omega)$ the imaginary part as well as ω the angular frequency. Since it is challenging to solve the integral Eq. (1) analytically, in practical validity tests, a K-K compliant model consisting of amounts of RC-elements in series is adapted to fit the measured impedance data set [50], and the relative residuals are expressed as:

$$\mathrm{Res\_Re}(\omega)=\frac{\mathrm{ReZ}(\omega)-\mathrm{Re}\hat{Z}(\omega)}{|Z(\omega)|} \qquad \mathrm{Res\_Im}(\omega)=\frac{\mathrm{ImZ}(\omega)-\mathrm{Im}\hat{Z}(\omega)}{|Z(\omega)|} \tag{2}$$

where $|Z(\omega)|$ indicates the absolute value of the measured data while $\hat{Z}(\omega)$ the model impedance. When the relative residuals are less than 1%, the measured impedance data is assumed to satisfy the K-K constraints of Eq. (1). The K-K test based on a LIN-KK tool [51] is employed to fit each measured impedance data.

2.3 Distribution of relaxation times

The relation between the DRT function and the impedance is expressed in [50] as:

$$Z(\omega)=R_0+R_{pol}\int_0^{\infty}\frac{\gamma(\tau)}{1+\mathrm{j}\omega\tau}\mathrm{d}\tau \tag{3}$$

where R_0 represents the ohmic resistance and R_{pol} the polarization resistance, while $\gamma(\tau)$ indicates the distribution function of relaxation times as well as τ the time constant of a single RC element. In the impedance spectrum, R_0 is defined as the high-frequency ($f\to\infty$) intercept with the real axis and R_{pol} the difference between the low-frequency ($f\to0$) and high-frequency ($f\to\infty$) intercept with the real axis.

For discrete calculation from the measured data set, the continuous function of Eq. (3) are

typically transferred into Eq. (4):

$$Z(\omega)=R_0+R_{pol}\sum_{k=1}^{N}\frac{\gamma_k}{1+j\omega\tau_k} \quad (4)$$

where *N* is the number of RC elements. When calculating DRT from the impedance data, Tikhonov regularization is key progress to determine regularization level [52] by the regularization parameter, which is set as 10^{-3} in this paper.

3. Results and discussion

3.1 Inconsistency cells in the stack

To explore the causes of unexpected performance degradation or shutdowns due to changes in operating conditions during a long-running, cell inconsistency becomes noteworthy in this stack. It can be noted that in Fig. 2a that, before this sack conducts EIS measurements, it has been operated over one year in succession from calendar time. Thereinto, the stack began to operate in April 2017 and proceeded with the EIS tests for the single cells in June 2018. During this time interval, the stack was mainly conducted the typical performance tests and the polarization curve tests. Moreover, the cells have a good consistency according to voltage responses at the beginning-of-test (BoT) in Fig. 2b. Therefore, all the cells can be considered as normal ones at beginning of tests even though their voltages show a tiny inconsistency. It is, for this small distinction inside the stack, caused by the difference of pressure loss in the manifold of fluids, the temperature difference of the cells, and the errors of some stochastic processes. In this study, the inconsistency among cell voltages gets significant of the stack in Fig. 2b after the stack operated for a period. It can be noted that the voltage responses of several cells (number 3, 8, 19 and 25) perform worse than the others at the load of 100 A and even worse at 150 A.

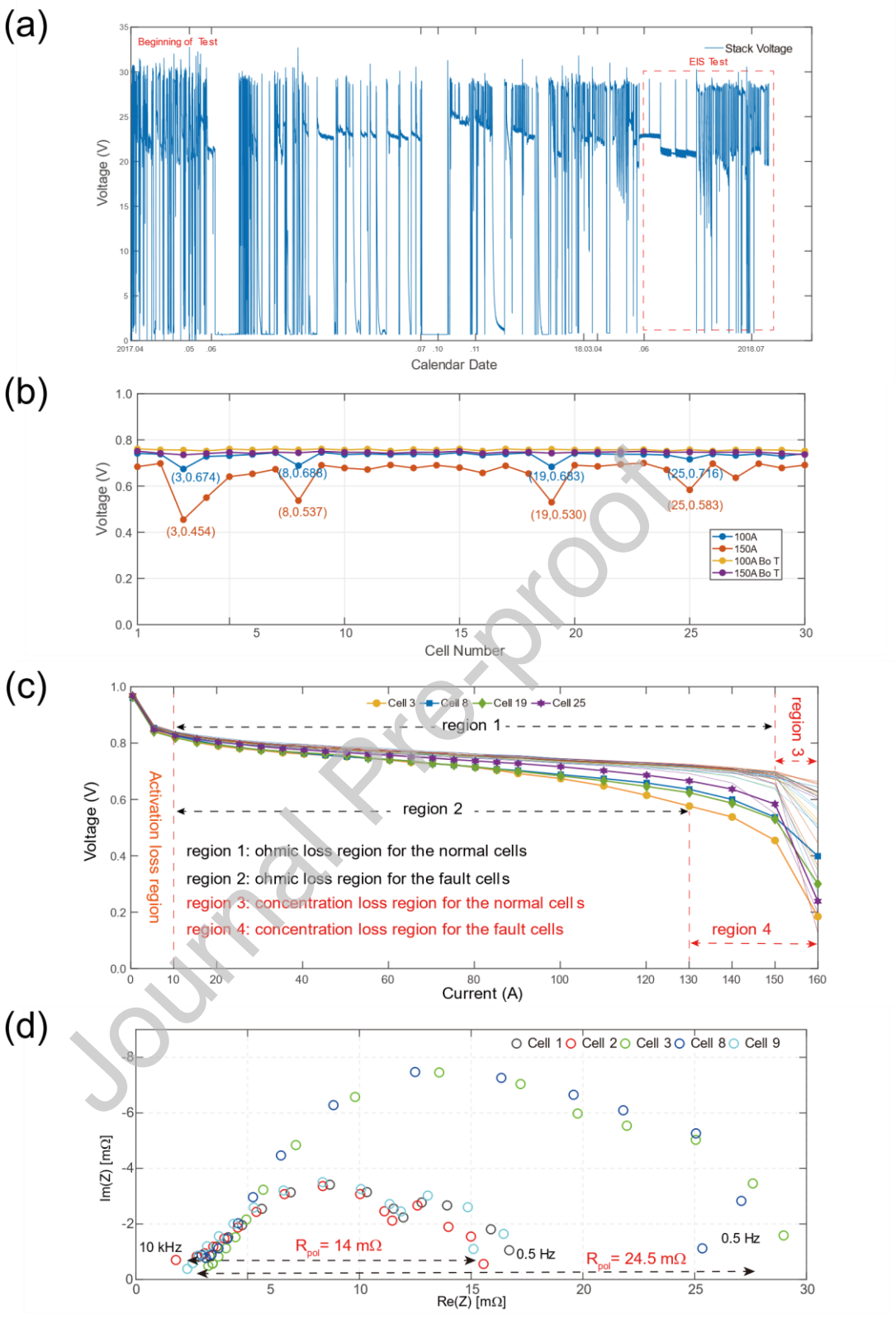

Fig. 2 a) The long-term running curves of this stack from 2017.04 to 2018.07 in calendar time, and the cell inconsistency of b) voltage responses at beginning-of-test and the at test time after a period, c) polarization curves, and d) impedance spectra of selected cells, in the PEMFC stack, where the data are recorded at the conditions of T_{ST}=60 °C, S_A=2.0, and S_C=2.5.

To deeply explore the performance dissimilarities due to cell inconsistencies, the inconsistency is further confirmed by the polarization curves of 30 cells and impedance spectra of 5 cells illustrated as Fig. 2c and 2d. From Fig. 2c, even though the voltage performance of a single cell resembles from 0 A to 80 A (including activation region and partial ohmic region), with current increasing, the cells (number 3, 8, 19 and 25) step into the concentration loss region from the ohmic loss region (region 2: 10~130 A) earlier than the others do (region 1: 10~150 A). Moreover, the voltage performance of the cells (number 3, 8, 19 and 25) declines rapidly since 120 A while the others begin from 150 A, and the inconsistency becomes even more distinct. In summary, the cells of numbers 3, 8, 19 and 25 are fault cells in this stack, while others are normal ones. In addition, the Nyquist plots in Fig. 2d depict the inconsistency as well, that fault cells (number 3 and 8) have larger polarization resistances (R_{pol}=24.5 mΩ) compared with the normal (R_{pol}=14 mΩ).

3.2 Analysis of DRT feasibility for large-scale PEMFCs

To extract the impedance information including eigenfrequency and eigenvalue in the Nyquist plot, DRT calculations are utilized to analyze the impedance characterization, reflecting the electrochemical process comprehensively and intuitively.

As mentioned in Section 2.2, EIS measurement is susceptible to noise, especially for the PEMFC with a large active area. The measured results accompany errors usually and even cannot reflect the impedance characteristics of PEMFCs in some cases. Hence, it is essential to validate the accuracy of the measured EIS before fitting the EIS based on the Kramers-Kronig relationship, i.e. the relative residuals between the measured EIS and the K-K fitted EIS is less than 1% according to Section 2.2. Only if satisfying such K-K constraints, the measured results are convincing in this paper. Previous studies [38], [41] have successfully applied the DRT methodology in fuel cells with a small active area,

demonstrating the EIS testing accuracy under ambient noise. In this paper, the authors conduct a series of EIS tests for large-scale cells tentatively and verify the accuracy of these measurements based on mathematical theories.

An example of the impedance spectra for cell 2 and cell 8 (operated at T_{ST}=60 °C, S_A=2.0, S_C=2.5, and the ohmic loss region at 100 A) is illustrated and analyzed in Fig. 3a and 3b. The former displays the Nyquist plots and the latter shows the residuals between the experimental and fitting, respectively. Good quality of the fitting curves and all the residuals less than 0.5% can be seen from Fig. 3a and 3b. Therefore, the measured result is convincible and proves the applicability of EIS measurement applying in large-scale PEMFCs as well.

After the above validity test, the DRT calculation is applied to analyze the EIS data in the 5 kW PEMFC stack for the first time. In Fig. 3c, the distribution function shows the inconsistencies between cell 2 and cell 8 with details: p1-10 Hz and p2-800 Hz for cell 2, p1-70 Hz and p2-400 Hz for cell 8, and p3-10 kHz for both cells. Furthermore, a small peak p0 in DRT analysis can be noted for cell 2 while for cell 8 it disappeared. In addition to the inconsistency of eigenfrequency, the eigenvalue of the distribution function of cell 8 is larger than that of cell 2 at p1 and p2. According to the advanced impedance study [38], the peaks in DRT analysis are allocated to the corresponding processes: p1 - gas diffusion process of oxygen in porous media layer, p2 - oxygen reduction reaction (ORR) correlated to charge kinetics, and p3 - proton transport at catalyst layer (CL) as well as p0 - water transport in the membrane [53]. Moreover, the above-mentioned is cathode electrochemical process while the anode not in consideration due to the small values of each peak. This paper focuses on the capacitive behaviors in DRT analysis and the discussion of low-frequency region - p0 is neglected.

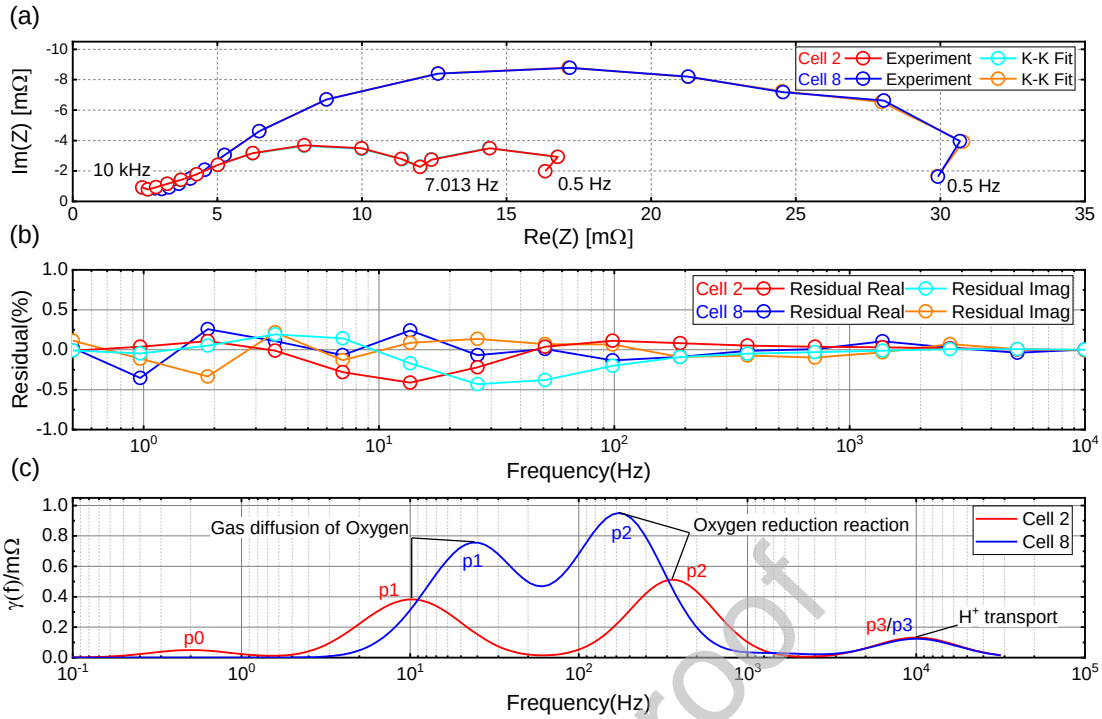

Fig. 3 (a) Impedance data and K-K fit recorded at T_{ST}=60 °C, S_A=2.0, S_C=2.5 and 100 A. (b) Residuals according to Kramers-Kronig validity. (c) Calculated distribution function in the frequency domain and the designation of peaks.

Based on the feasibility, the comparative investigation including impedance spectrum, DRT distribution function, and voltage are discussed in the following sections to investigate the inconsistent responses on operating conditions of the PEMFC stack.

3.3 Inconsistent responses on operating conditions

Generally, cell location, operating conditions and running strategies result in cell inconsistency during PEMFC stack running. Nevertheless, severe operating conditions (overheating, reactant starvation, etc.) promote performance degradation even lead to materials damage, accelerating the inconsistency. In this section, cell 2 representing the normal cell, and cell 8 the fault cell are compared to investigate the response characteristics under operating conditions.

3.3.1 Inconsistent responses on stack temperature

Fig. 4 gives a graph review of the impedance data and corresponding DRTs of cell 2 and cell 8 with the temperature altering. To have a better overview of inconsistent responses on temperature

parameters, the impedance spectra and distribution function curves are subdivided into three and two scopes, respectively. Fig.4a and b show the Nyquist plots and corresponding distribution functions for stack temperatures from 35 °C to 70 °C. Fig. 4c and d illustrate the enlarged graph for the real axis range from 0 to 20 mΩ and 2.0 to 4.0 mΩ, respectively, and Fig. 4e displays the amplified region of p3.

At each temperature, cell 2 and cell 8 can be distinguished by the polarization resistance for Fig. 4a, the eigenvalue and the corresponding eigenfrequency of distribution function for Fig. 4b. The polarization resistance R_{pol} for cell 8 is more than 21 mΩ, while for cell 2 is less than 16 mΩ. Hence, normal and faulty cells can be preliminarily discriminated from the Nyquist plot. In Fig. 4b, the differences of the eigenvalues for p1 and p2 are intuitive, especially for p1, the eigenvalue of cell 8 is much larger than that of cell 2. Although the eigenvalue of p2 is approximative at the temperature of 70 °C, the differences are distinct at low temperatures. In addition, the eigenfrequency, e.g. at 70 °C, of cell 8 is larger at p1-70 Hz and smaller at p2-700 Hz compared with that of cell 2. Combined with the electrochemical processes of oxygen diffusion and ORR expressed by p1 and p2, respectively, it can be noted that oxygen diffusion and ORR are more difficult in fault cells due to larger eigenvalues. In this paper, the damaged internal structure for fault cells is assumed the reason for this difference.

Inconsistent responses exist in single cells on temperature, i.e. cell response changes with stack temperature altering, especially for the fault cells. For the Nyquist plot of cell 8, the value of polarization resistance decreases from 44 mΩ to 21 mΩ with stack temperature increasing, and the ohmic resistance changes ranged from 2.8 mΩ to 3.4 mΩ. The great changes in polarization resistance, particularly in the case below 50 °C, indicate that fault cells are sensitive to low temperatures. To explore the changes of the corresponding processes with stack temperature, Fig. 4b illustrates the DRTs for cell 8 under each temperature. With stack temperature increasing, the eigenvalue declines obviously

from 2.04 mΩ to 0.67 mΩ of p1, and from 1.55 mΩ to 0.73 mΩ of p2, as well as corresponding eigenfrequency right shifts from 10 Hz to 70 Hz, and from 111 Hz to 700 Hz, respectively. In addition, the value of p3 has little changes with temperature varying. One explanation for these results is water content in the MEA and temperature affects reaction velocity. At low temperatures such as 35 °C and 40 °C, the produced water by ORR condensing droplets even forming water plugs accumulates around the porous layers and blocks the pores. Therefore, it is hard for oxygen to diffuse through GDL and CL, even for water to be removed outside. Moreover, the water remained in MEA causing the medium change, which affects the value of double-layer capacitance, leads to the right shifting of eigenfrequency ultimately.

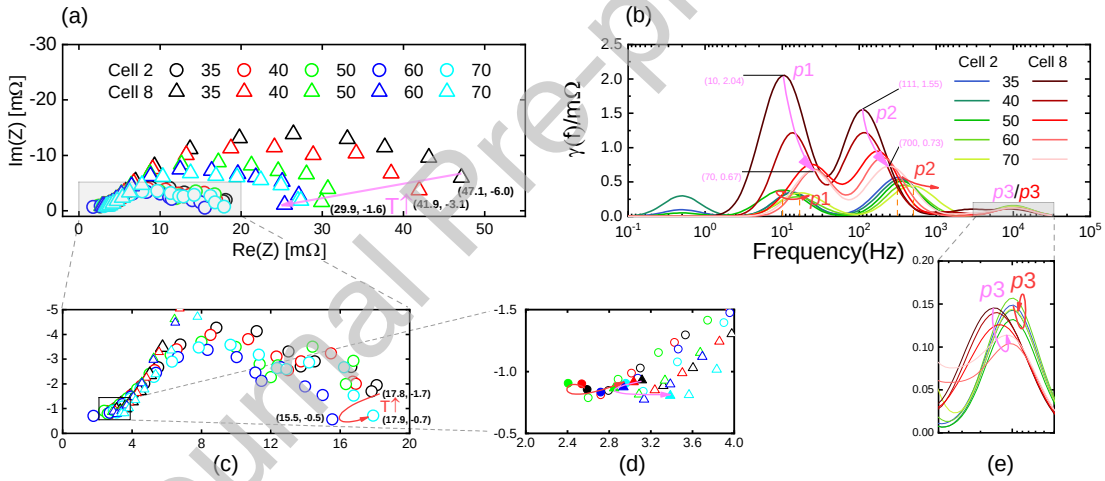

Fig. 4 (a) Impedance data recorded at stack temperature measurements while other parameters of S_A=2.0, S_C=2.5 and 100 A keep constant. (b) Corresponding DRTs. (c) Enlarged graph of the impedance data of Cell 2. (d) Enlarged graph of the high-frequency impedance data. (e) Enlarged graph of DRTs at p3 region.

Similarly, cell 2 responds inconsistently to stack temperature as well, which can be demonstrated by the results in Fig. 4b and c. The value of polarization resistance has minor decreases from 15 mΩ to 13 mΩ with stack temperature increasing, and the ohmic resistance increases from 2.4 mΩ to 3.0 mΩ. In Fig. 4b, temperature changing has little effect on the electrochemical processes for normal cells. With the temperature increasing, the eigenfrequency has a right shifting from 10 Hz to 50 Hz of p1 and from 800 Hz to 900 Hz of p2, and the eigenvalue of p2 decreases a little from Fig. 4b. The frequency

shifting of p1 and p2 indicates that water accumulating in the porous layers, leading to the medium change and affects the double-layer capacitance. The decease of p2 can be explained by that despite the water accumulating in CL, the increased temperature accelerates electrochemical reaction and makes ORR easy to occur.

The above results represent that the cell responds inconsistently to stack temperature. However, it can be found that the responses of normal and faulty cells on stack temperature are inconsistent through their comparison. The inconsistencies are as follows: (i) In Fig. 4a and c, R_{pol} of cell 8 declines the most about 12 mΩ at stack temperature from 40 °C to 50 °C, while of cell 2 only reduces several mΩ under temperature altering. The inconsistency of EIS with temperature changing between cell 2 and cell 8 can be proved by the structural inconsistency of MEA, where the fault cell has a poor MEA in the stack after a long operation. (ii) In Fig. 4b, the varying of the eigenvalue for p1 and p2 demonstrates that cell 8 has a worse porosity of GDLs and CLs. Excessive water at low temperatures blocks the pores of GDL and CL, impeding the processes of oxygen diffusion and water removal. However, cell 2 performs the opposite, which can be deemed as that plenty of free pores of GDL and CL provide paths for water molecule and oxygen. (iii) In Fig. 4b, with stack temperature increasing, the range of eigenfrequency shifting is p1-40 Hz and p2-100 Hz for cell 2 and p1-60 Hz and p2-600 Hz for cell 8, respectively. Frequency inconsistency indicates that water is prone to stay in the MEA of fault cells, accelerating the structure degradation and performance decrease.

Overall, the responses of cells in the stack are inconsistent on temperature. This inconsistency not only exists in the cathode electrochemical process of single cells, but also represented in the responses between the normal and faulty cells. In addition, both oxygen diffusion and ORR processes are sensitive to the operating conditions of low temperatures.

3.3.2 Inconsistent responses on anode stoichiometric (S_A)

Fig. 5 shows the results at the parameter of anode hydrogen stoichiometric. Fig. 5a gives an overall view for the Nyquist plot and Fig. 5c, d the enlarged graph in the high-frequency and low-frequency region, respectively. Furthermore, Fig. 5b represents the corresponding DRT calculations and the enlarged graphs Fig. 5e, f in p2 and p3 region for a better view.

In general, the Nyquist plot in Fig. 5a reveals that cell 2 and cell 8 can be distinguished intuitively by polarization resistance. At these operating condition tests, the mean value of polarization resistance R_{pol} of cell 8 is 18.4 mΩ, while of cell 2 is 11.2 mΩ. Moreover, it can be seen from Fig. 5b that the mean eigenvalue of p1 is about 0.3 mΩ for cell 2 and 0.5 mΩ for cell 8, and of p2 is about 0.36 mΩ for cell 2 and 0.7 mΩ for cell 8. From the overview of EIS and DRT analysis, the normal and fault cells are identifiable in the stack.

To explore the responses of cells on anode hydrogen stoichiometric, little inconsistency can be found from EIS and DRT analysis. EIS plot resembles cell 2 from S_A=2.0 to S_A=1.1 with no distinct differences shown in Fig. 5a. However, the enlarged graph Fig. 5c represents that ohmic resistance (R_0=2.37 mΩ) at S_A=2.0 is larger than that of other conditions (R_0=2.12 mΩ). Approximately, cell 8 follows the regularity of cell 2, where the ohmic resistance (R_0=2.79 mΩ) at S_A=2.0 but at other conditions R_0=2.56 mΩ. The inconsistency of ohmic resistance at a high fuel inlet flow rate indicates that excess hydrogen enhances cell performance little, even the unreacted hydrogen molecule diffuses back to the channel to be removed accompanying with water molecular inside the membrane, causing localized dehydration and decreased proton conductivity. In addition, EIS and DRT analysis in Fig. 5b of cell 8 show that polarization resistance and the eigenvalue of p1 increase at S_A=1.1, respectively. In this case, it can be explained that insufficient hydrogen slows down the reaction, thus leading to a small

increase in oxygen diffusion resistance.

Several inconsistent responses between cell 2 and cell 8 on hydrogen stoichiometric can be noted despite little changes in EIS and DRT. DRT analysis reveals more information about the changes of both cells. The range of peak values for cell 2 and cell 8 is inconsistent in Fig. 5b: (i) The range of cell 2 is that p1 0.259 ~ 0.317 mΩ and p2 0.357 ~ 0.372 mΩ. (ii) The range of cell 8 is that p1 0.443 ~ 0.541 mΩ and p2 0.682 ~ 0.763 mΩ. Through the above results and the EIS plots, it can be noted that cell 8 is sensitive to the changes of hydrogen stoichiometric, even for cell 2 the phenomena are not obvious.

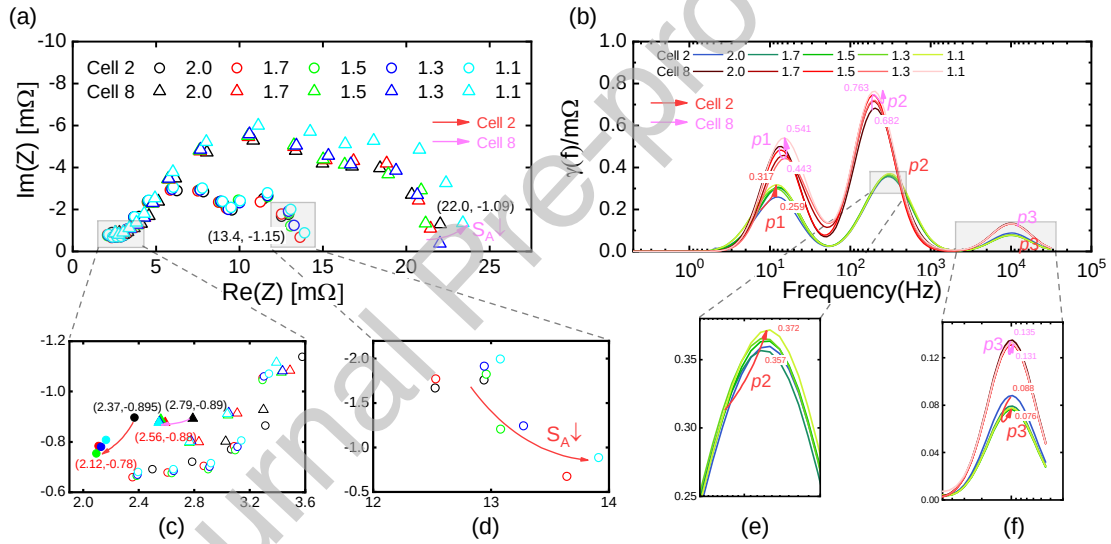

Fig. 5 (a) Impedance data of cell 2 and cell 8 recorded at anode hydrogen stoichiometric measurements while other parameters of T_{ST}=60 °C, S_C=2.5, and 100 A keep constant. (b) Corresponding DRTs. (c) The enlarged graph in the high-frequency region. (d) The enlarged graph of cell 2 in the low-frequency region. (e) The enlarged graph of DRTs at p2 region for cell 2. (f) Enlarged graph of DRTs at p3 region.

The results under this case demonstrate that cells in the stack have a few inconsistent responses on hydrogen stoichiometric. However, the ohmic resistance can be reduced by excessive hydrogen. Moreover, the tolerant capacity for condition changes of fault cells is not as good as the normal ones due to their damaged structure. Therefore, the stack, especially the fault cells inside, should be carefully operated for high performance.

3.3.3 Inconsistent responses on cathode stoichiometric (S_C)

Measurement results with varied cathode air stoichiometric S_C from 3.0 to 1.7 are displayed in Fig. 6. Fig. 6a shows the impedance spectra of both cells and the enlarged graphs Fig. 6c, d for a better view. Corresponding DRT analysis is given in Fig. 6b with an enlarged p2 region Fig. 6e.

Cell 2 and cell 8 are easily identified by the impedance data, the shape of EIS, and the eigenvalue of oxygen diffusion in Fig. 6a and b. Although the results in Fig. 6d indicate that the ohmic resistances for both cells, in this case, are almost constant. The real and imaginary part of impedance data shows that cell 8 is the fault cells due to the large impedance (about three times that of cell 2) at low air stoichiometric. Moreover, the inconsistency of eigenvalues of p1 noted in Fig. 6b enhances the result that the structure of cell 8, especially for the cathode GDL, is damaged compared with cell 2.

In addition to the results of identifying cell state through EIS and DRT analysis, the inconsistent responses of single cells can be noted as well. With S_C decreasing, the impedance including the real and imaginary parts shows a great increase of the recorded data at low frequency. For cell 2 in Fig. 6c, the low-frequency impedance increases from 13.5 mΩ to 24.1 mΩ for the real part and from -0.75 mΩ to -3.18 mΩ for the imaginary part, where the growth trend as the red arrow shows. It is notable in Fig. 6a that the imaginary part of cell 8 impedance increases exponentially from -1.61 mΩ at S_C=3.0 to -30.5 mΩ at S_C=1.7. The real part of cell 8 increases from 20.4 mΩ to 56.2 mΩ likewise. Furthermore, the spectra shape of cell 8 varies greatly from an arc to a straight line in the low-frequency region with air stoichiometric declining.

Fig. 6b reveals that p1 is severely affected by air stoichiometric, especially for cell 8. With S_C declining, a rise up of p1 eigenvalue are from 0.46 mΩ to 4.13 mΩ and its eigenfrequency shifts from 50 Hz to 7 Hz for cell 8, respectively. The eigen-parameters of cell 2 are from 0.29 mΩ to 0.95 mΩ and

from 30 Hz to 9.5 Hz, individually. Oxygen insufficiency cannot provide competent forces to drive oxygen diffusing through GDL and MPL to the reacting place. Besides, the produced water failed to be removed timely occupies most pores, increasing the difficulty for the diffusion process and change the medium of microporous layers. In addition, p2 shows a little variety at the measurements in Fig. 6e: (i) The eigenvalue increases from 0.79 mΩ to 1.08 mΩ with eigenfrequency shifting from 600 Hz to 200 Hz for cell 8. (ii) About 0.07 mΩ increase of the eigenvalue in Fig. 6b and 150 Hz shifting during S_C decreasing from 3.0 to 1.7 represented in Fig. 6e for cell 2. For the changes of p2, oxygen starvation and water content at low air stoichiometry impede the ORR process for cell 8 due to the poor porosity, while for cell 2 structural integrity helps to avoid this phenomenon.

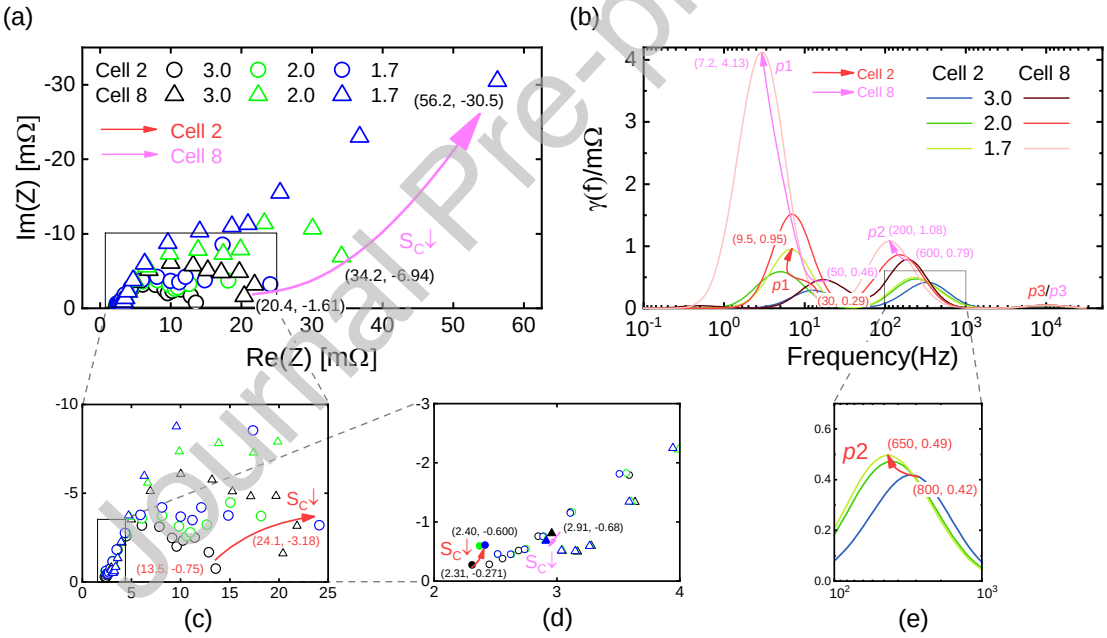

Fig. 6 (a) Impedance data of cell 2 and cell 8 recorded at cathode air stoichiometric measurements while other constant parameters of T_{ST}=60 °C, S_A=2.0, and 100 A (ohmic region). (b) Corresponding DRTs. (c) The enlarged graph in the region of ~ 25 mΩ. (d) The enlarged graph of the high-frequency region. (e) The enlarged graph of DRTs at the p2 region for cell 2.

Results through the comparison investigation demonstrate the inconsistent responses between cell 2 and cell 8 on air stoichiometric. The followings are the detailed inconsistencies between cell 2 and cell 8. With the air stoichiometric declining, the increase of polarization resistances calculated from Fig.

6a and care 32.8 mΩ for cell 8 while 8.2 mΩ for cell 2, respectively. The imaginary part of the low-frequency impedance increase is 28.9 mΩ for cell 8 while 2.43 mΩ for cell 2 in Fig. 6a and c. Moreover, Fig. 6b shows that the increase of the p1 eigenvalue of cell 8 is 3.6 mΩ, which is much larger than 0.65 mΩ of cell 2. The inconsistency values of impedance parameters and DRT analysis and frequency shift between cells indicate that the damaged MEAs especially cathode GDL and CL contribute to the poor characteristics of fault cells. Furthermore, the sensitivities to cathode air changes, e.g., insufficient air inlet can be owned to the damaged structure of GDLs and CLs as well.

In conclusion, the oxygen diffusion process is sensitive to air shortage and air changes, which causes inadequate forces driving gases through porous layers as well as drag water outside. For the cells, the structural weakness of fault cells mainly owns to the poor capacities of water removal and gas diffusion compared with normal ones.

3.3.4 Voltage responses on operating conditions

Above Nyquist plots and DRT analysis investigate the static characteristics of the cells, while not reveal the dynamic characteristics during EIS measurements. Therefore, Fig. 7 illustrates the dynamic performance of selected cells and the stack, where Fig. 7a displays the measurements at the stack temperature condition, Fig. 7b the anode hydrogen stoichiometric parameter, and Fig. 7c the cathode air stoichiometric variable, respectively. Moreover, the average voltage is shown as well to analyze voltage variation trends with conditions altering. In order of the cell number (cell 1, 2, 3, 8 and 9), five EIS tests are conducted under each condition in the process of 15 minutes. Thereinto, the mean value of voltage response for single cells and the stack is calculated by the following expression:

$$EV_{\mathrm{k}} = \frac{1}{60\times 2\times T}\sum_{i=1}^{60\times 2\times T} V_{\mathrm{k},\,i} \quad (\mathrm{k} = \text{stack, cell 2, cell 8}) \tag{5}$$

where EV is the average voltage, T, with the unit of minute, denotes the time interval during the EIS

test under each operating condition, *i* represents the *i*th voltage data recorded by the test bench, and k denotes the objective of single cells and the stack, respectively.

As shown in Fig. 7, performance inconsistency exists between cells and the stack during operating. Cells perform steadily most of the time and fluctuate at impedance testing only, contrast with the cells, the stack voltage undulates through the entire process not only impedance tests. The results in Fig. 7 represent the relationships of the stack to normal and fault cells, as well as the similarities and differences between cells, with details as follows.

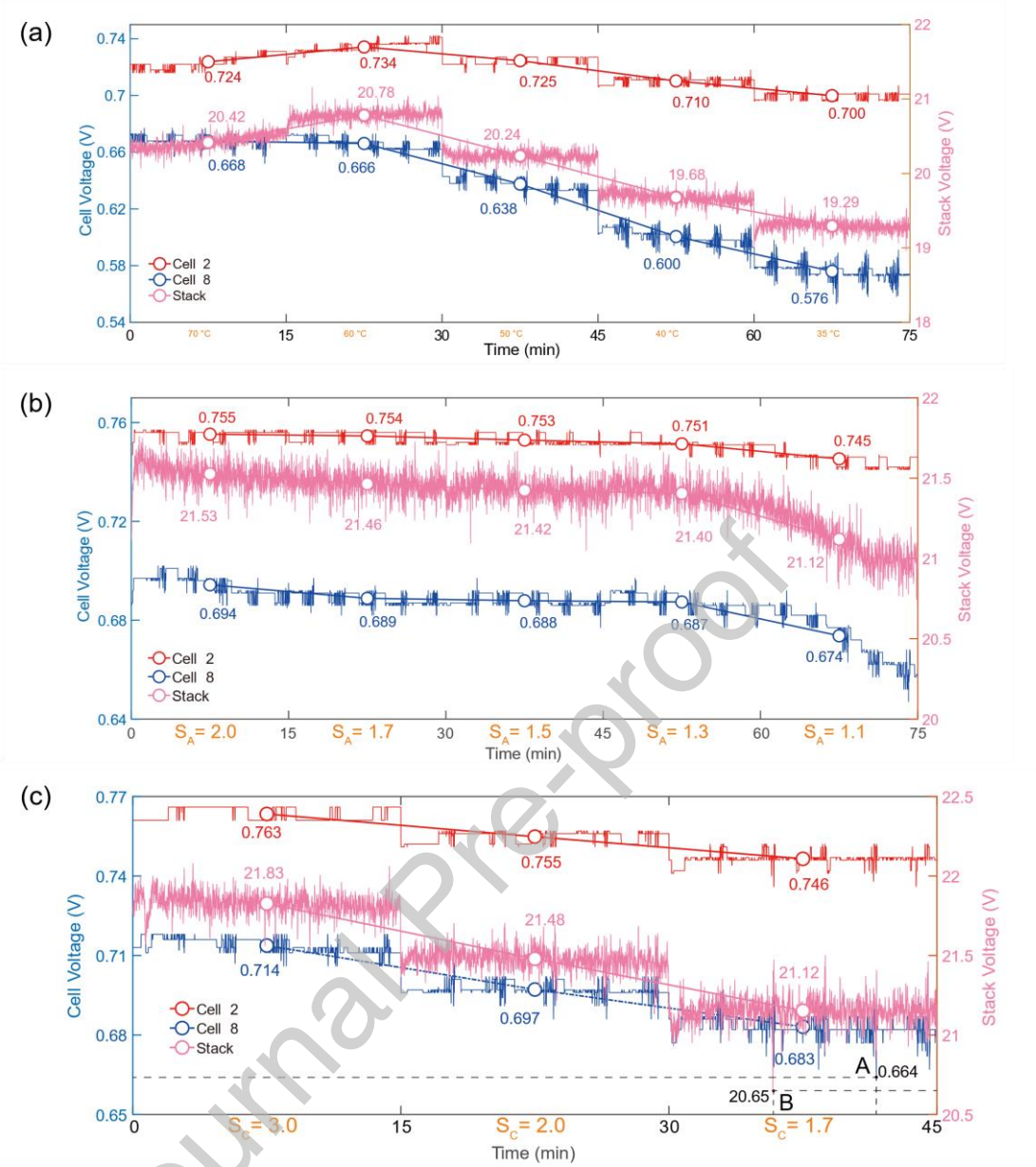

Fig. 7 Voltage responses of cells and stack at the measurements of (a) temperature conditions from 70 °C to 35 °C in Section 3.3.1. (b) anode hydrogen stoichiometric from 2.0 to 1.1 in Section 3.3.2. (c) cathode air stoichiometric from 3.0 to 1.7 in Section 3.3.3.

Under the temperature condition, Fig. 7a indicates that the stack has a similarity of increasing performance with cell 2 when condition decreasing to 60 °C, the voltage downtrend is getting larger at low temperature, and cell 8 fluctuates enhanced during the EIS measurements at 35 °C. Only a little performance decrease of 0.03 V for cell 2, 0.07 V for cell 8, and 0.13V for the stack, respectively, exist for both cell and stack at S_{AH} conditions from 2.0 to 1.3 in Fig. 7b. However, inadequate hydrogen at S_A=1.1 leads to a voltage drop even sustained declines during running, especially for cell 8 and the

stack. It is shown in Fig. 7c that the amplitude of voltage waves at EIS measurements increases gradually with S_{CA} declining, particularly under oxygen starvation. Moreover, the minimum value of voltage is only about 0.664 V and 20.65 V for cell 8 and the stack despite having a good average performance of 0.683 V and 21.15 V, respectively.

Performance inconsistencies including cell inconsistencies of steady performance, responses on current disturbance and voltage changing trend, and inconsistency between cells and stack indicate that fault cells are sensitive to operating conditions and small disturbances at severe conditions, as well as the stack perform unstably under insufficient fuel and oxygen starvation. According to the barrel effect in the stack and real-time monitoring, the operative conditions and superimposed current signal should be adequately considered to avoid sudden shut-ups during measurements.

3.4 MEA inconsistency

Section 3.3.1 to 3.3.4 explores the impedance and voltage responses of cells on operating conditions from the view of data characteristics. In order to understand the mechanism causing cell inconsistency, a visualization using the MEA component for comparison is conducted by JSM-7800F. The corresponding micrographs including membrane, flow channel, GDL and CL are displayed in Fig. 8.

Fig. 8a, the micrographs at 100× and 500× of the membrane, shows that several impurity clusters attach on membrane surface for both cells and fallen carbon fiber as well for the fault cell. Fig. 8b depicting the flow channel of 100× and 500× indicates that ribs and channels are holonomic and flat for the normal cell. However, impurities with a maximum width of 7.5 um on the channel and materials loss of ribs are observed in the fault cell. For the comparative micrographs in Fig. 8c, the porous structure of GDL composed of carbon paper and carbon rods can be clearly observed in the normal cell.

In contrast, in the image of the fault cell, partial pores are covered by CL materials and particles attached to the carbon rod, which leads to poor porosity. In Fig. 8d, CL fully covers the GDL with ordered distribution materials for normal cell, while for fault cell materials has fallen and passed through the pores to GDL. Moreover, most of the platinum is covered, causing the decreased effective surface of fault cells.

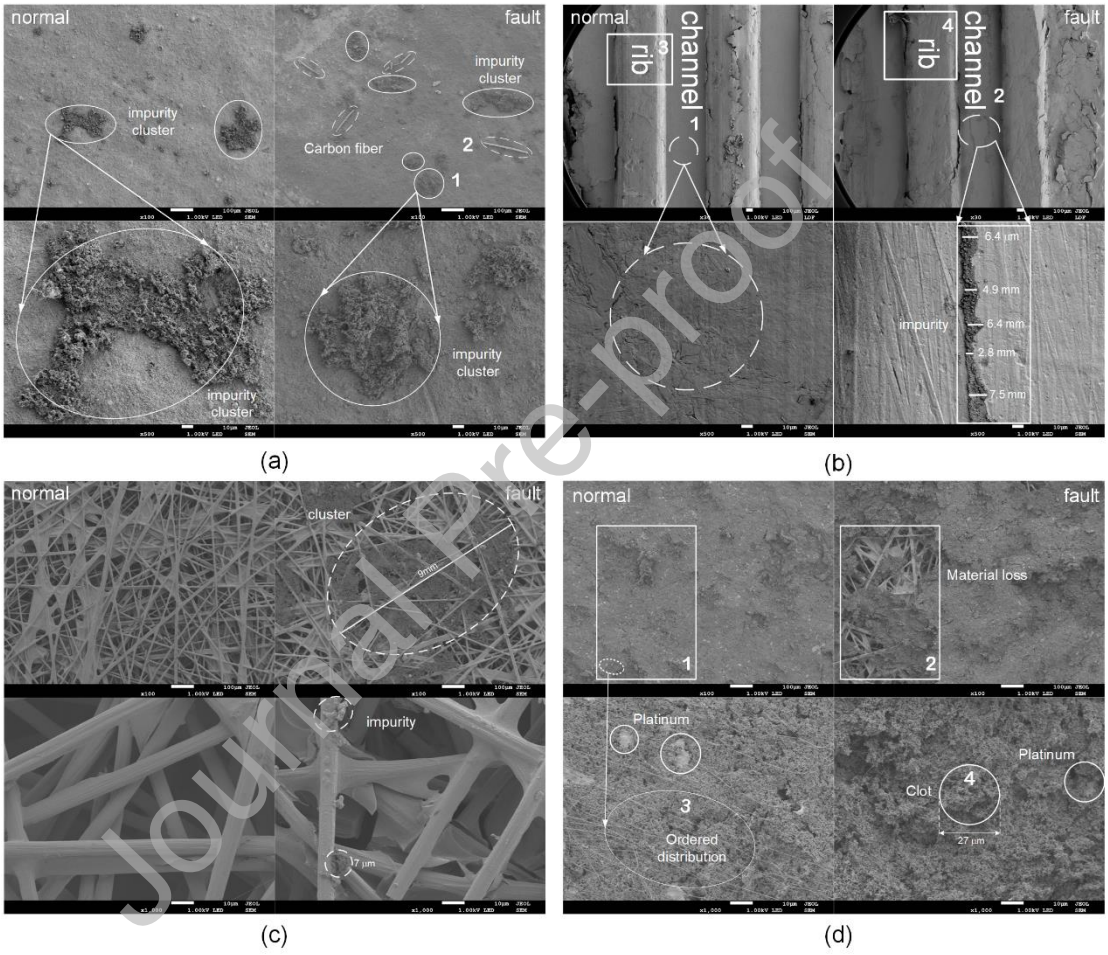

Fig. 8 Comparative micrographs of (a) membrane of 100× and 500×, (b) flow channel of 30× and 500×, (c) gas diffusion layer of 100× and 1000×, and (d) catalyst layer of 100× and 1000×, for the normal and fault cell.

The above analysis proves that structure inconsistency of the component among cells exists even they are running under the same condition. Noted that fault cells have poor MEA components and flow field after long-term operation: (i) Impurities attached on the membrane and channel surface resist the transport process of the proton, reactant, and water. (ii) Material abscission leads to structural

inconsistency and non-uniform reaction. For instance, cross flows exist due to the rib material abscission and water accumulation accumulates due to material abscission. (iii) Diffusion process slows down caused by the blocked surface of GDL and the reaction process decreases due to the reduced effective reaction surface. Hence, to reduce or avoid the consistency phenomena in the stack, the cells and operating conditions should be protected and adjusted in the running process, respectively.

4. Conclusion

Cell inconsistency is observed in a 5 kW PEMFC stack under different working conditions. A comprehensive strategy is proposed in this paper to investigate inconsistency details and mechanisms between normal and faulty cells, which includes steady performance, polarization curve, EIS with DRT analysis, and SEM visualization. The accuracy of EIS measurement applied to large-scale PEMFCs is validated by the Kramers-Kronig test. In all cases, two selected cells with 312 cm^2 active area are conducted under three types of measurements (stack temperature, hydrogen stoichiometric, and air stoichiometric) to comparatively explore the inconsistent responses on operating conditions.

The inconsistent polarization curves indicate that fault cells have a worse performance under high current densities with more generated water. Responses on low temperature and low air stoichiometric further confirm fault cells perform poorly under plenty of water content. Moreover, inconsistent voltage responses demonstrate fault cells performance are lower than the normal ones, sensitivity to condition changes, and even sensitivity to the superimposed signal at severe conditions. EIS and DRT analysis detail the specific inconsistencies including impedance and the electrochemical process of oxygen diffusion and ORR. In this case, cell inconsistent responses on operating conditions suggest that temperature affects both oxygen diffusion and ORR while air supply mainly contributes to the oxygen diffusion process. Inconsistent responses between cells indicate fault cells have a poor electrochemical

process, especially oxygen diffusion, and verify fault cells are sensitive to water in PEMFC. The inconsistencies of external performance and detailed internal characteristics are confirmed by the structural inconsistencies of MEA between normal and faulty cells. Blocked pores of GDLs, damaged CLs and covered platinum particles all confirm the reason why fault cells perform worse from the mechanism perspective. It can be derived from experimental results that cell inconsistency occurs in the stack even cells at the same conditions, and inappropriate conditions accelerate this inconsistency. Therefore, the running strategy and drainage system should be improved in large-scale stacks to protect poor cells, avoid severe fault states, reduce cell inconsistency, and improve PEMFC durability.

Credit author statement

Review & Editing, Supervision, Project administration, Funding acquisition.

Jiang Yu: Methodology, Software, Formal Analysis, Data Curation, Investigation, Writing- Original Draft, Visualization.

Huang Lei: Formal Analysis, Data Curation, Investigation.

Chen Weirong: Resources, Writing- Review & Editing, Supervision, Project administration.

Dan Brett: Writing- Review & Editing, Supervision

Declaration of interests

☒ The authors declare that they have no known competing financial interests or personal relationships that could have appeared to influence the work reported in this paper.

Acknowledgements

This work is supported by the National Natural Science Foundation (No. 51607149), Department of Science and Technology of Sichuan Province (No.2019YJ0236), and Key Laboratory of Magnetic Suspension Technology and Maglev Vehicle, Ministry of Education.

We would like to thank Analytical and Testing Center of Southwest Jiaotong University for their assistance with PEMFC SEM analysis.

References

[1] J. Zhao, X. Li, A review of polymer electrolyte membrane fuel cell durability for vehicular applications: Degradation modes and experimental techniques, Energy Convers. Manag. 199 (2019) 112022. https://doi.org/10.1016/j.enconman.2019.112022.

[2] P. Corbo, F. Migliardini, O. Veneri, Performance investigation of 2.4kW PEM fuel cell stack in vehicles, Int. J. Hydrogen Energy. 32 (2007) 4340–4349. https://doi.org/10.1016/j.ijhydene.2007.05.043.

[3] P. Corbo, F. Migliardini, O. Veneri, Experimental analysis of a 20 kWe PEM fuel cell system in dynamic conditions representative of automotive applications, Energy Convers. Manag. 49 (2008) 2688–2697. https://doi.org/10.1016/j.enconman.2008.04.001.

[4] T. Ruiu, A.M. Dreizler, J. Mitzel, E. Gülzow, Evaluation of a 2.5 kWel automotive low temperature PEM fuel cell stack with extended operating temperature range up to 120 °C, J. Power Sources. 303 (2016) 257–266. https://doi.org/10.1016/j.jpowsour.2015.10.056.

[5] G. Giacoppo, S. Hovland, O. Barbera, 2 kW Modular PEM fuel cell stack for space applications: Development and test for operation under relevant conditions, Appl. Energy. 242 (2019) 1683–1696. https://doi.org/10.1016/j.apenergy.2019.03.188.

[6] T. Özgür, A.C. Yakaryılmaz, A review: Exergy analysis of PEM and PEM fuel cell based CHP systems, Int. J. Hydrogen Energy. 43 (2018) 17993–18000. https://doi.org/10.1016/j.ijhydene.2018.01.106.

[7] M. Bornapour, R.-A. Hooshmand, M. Parastegari, An efficient scenario-based stochastic programming method for optimal scheduling of CHP-PEMFC, WT, PV and hydrogen storage units in

micro grids, Renew. Energy. 130 (2019) 1049–1066. https://doi.org/10.1016/j.renene.2018.06.113.

[8] L. Dubau, L. Castanheira, F. Maillard, M. Chatenet, O. Lottin, G. Maranzana, J. Dillet, A. Lamibrac, J.-C. Perrin, E. Moukheiber, A. ElKaddouri, G. De Moor, C. Bas, L. Flandin, N. Caqué, A review of PEM fuel cell durability: materials degradation, local heterogeneities of aging and possible mitigation strategies, Wiley Interdiscip. Rev. Energy Environ. 3 (2014) 540–560. https://doi.org/10.1002/wene.113.

[9] A. Mohammadi, A. Djerdir, N. Yousfi Steiner, D. Khaburi, Advanced diagnosis based on temperature and current density distributions in a single PEMFC, Int. J. Hydrogen Energy. 40 (2015) 15845–15855. https://doi.org/10.1016/j.ijhydene.2015.04.157.

[10] X. Wang, I.M. Hsing, Y.J. Leng, P.L. Yue, Model interpretation of electrochemical impedance spectroscopy and polarization behavior of H2/CO mixture oxidation in polymer electrolyte fuel cells, Electrochim. Acta. 46 (2001) 4397–4405. https://doi.org/10.1016/S0013-4686(01)00682-X.

[11] R. Makharia, M.F. Mathias, D.R. Baker, Measurement of Catalyst Layer Electrolyte Resistance in PEFCs Using Electrochemical Impedance Spectroscopy, J. Electrochem. Soc. 152 (2005) A970. https://doi.org/10.1149/1.1888367.

[12] N. Fouquet, C. Doulet, C. Nouillant, G. Dauphin-Tanguy, B. Ould-Bouamama, Model based PEM fuel cell state-of-health monitoring via ac impedance measurements, J. Power Sources. 159 (2006) 905–913. https://doi.org/10.1016/j.jpowsour.2005.11.035.

[13] S.K. Roy, M.E. Orazem, Analysis of flooding as a stochastic process in polymer electrolyte membrane (PEM) fuel cells by impedance techniques, J. Power Sources. 184 (2008) 212–219. https://doi.org/10.1016/j.jpowsour.2008.06.014.

[14] Z. Hu, L. Xu, J. Li, X. Xu, Z. Song, M. Ouyang, X. Du, The uniformity and consistency analysis

of a fuel cell stack with multipoint voltage-monitoring method, Energy Procedia. 158 (2019) 2118–2125. https://doi.org/10.1016/j.egypro.2019.01.486.

[15] R. Lin, Y. Zhu, M. Ni, Z. Jiang, D. Lou, L. Han, D. Zhong, Consistency analysis of polymer electrolyte membrane fuel cell stack during cold start, Appl. Energy. 241 (2019) 420–432. https://doi.org/10.1016/j.apenergy.2019.03.091.

[16] Z. Hu, L. Xu, J. Li, Q. Gan, X. Xu, M. Ouyang, Z. Song, J. Kim, A multipoint voltage-monitoring method for fuel cell inconsistency analysis, Energy Convers. Manag. 177 (2018) 572–581. https://doi.org/10.1016/j.enconman.2018.09.077.

[17] Y. Tang, W. Yuan, M. Pan, Z. Li, G. Chen, Y. Li, Experimental investigation of dynamic performance and transient responses of a kW-class PEM fuel cell stack under various load changes, Appl. Energy. 87 (2010) 1410–1417. https://doi.org/10.1016/j.apenergy.2009.08.047.

[18] J.-H. Jang, W.-M. Yan, H.-C. Chiu, J.-Y. Lui, Dynamic cell performance of kW-grade proton exchange membrane fuel cell stack with dead-ended anode, Appl. Energy. 142 (2015) 108–114. https://doi.org/10.1016/j.apenergy.2014.12.073.

[19] E. Pahon, N. Yousfi Steiner, S. Jemei, D. Hissel, P. Moçoteguy, A signal-based method for fast PEMFC diagnosis, Appl. Energy. 165 (2016) 748–758. https://doi.org/10.1016/j.apenergy.2015.12.084.

[20] Z. Li, C. Cadet, R. Outbib, Diagnosis for pemfc based on magnetic measurements and data-driven approach, IEEE Trans. Energy Convers. 34 (2019) 964–972. https://doi.org/10.1109/TEC.2018.2872118.

[21] Z. Li, R. Outbib, S. Giurgea, D. Hissel, Diagnosis for PEMFC Systems: A Data-Driven Approach With the Capabilities of Online Adaptation and Novel Fault Detection, IEEE Trans. Ind. Electron. 62 (2015) 5164–5174. https://doi.org/10.1109/TIE.2015.2418324.

[22] J.-M. Le Canut, R.M. Abouatallah, D.A. Harrington, Detection of Membrane Drying, Fuel Cell Flooding, and Anode Catalyst Poisoning on PEMFC Stacks by Electrochemical Impedance Spectroscopy, J. Electrochem. Soc. 153 (2006) A857. https://doi.org/10.1149/1.2179200.

[23] L. Ifrek, S. Rosini, G. Cauffet, O. Chadebec, L. Rouveyre, Y. Bultel, Fault detection for polymer electrolyte membrane fuel cell stack by external magnetic field, Electrochim. Acta. 313 (2019) 141–150. https://doi.org/10.1016/j.electacta.2019.04.193.

[24] A. Debenjak, M. Gašperin, B. Pregelj, M. Atanasijević-Kunc, J. Petrovčič, V. Jovan, Detection of flooding and drying inside a PEM fuel cell stack, Stroj. Vestnik/Journal Mech. Eng. 59 (2013) 56–64. https://doi.org/10.5545/sv-jme.2012.640.

[25] H. Chen, Y. He, X. Zhang, X. Zhao, T. Zhang, P. Pei, A method to study the intake consistency of the dual-stack polymer electrolyte membrane fuel cell system under dynamic operating conditions, Appl. Energy. 231 (2018) 1050–1058. https://doi.org/10.1016/j.apenergy.2018.09.184.

[26] Y. Li, Y. Li, X. Zhao, Z. Liu, W. Chen, Q. Li, Experimental study on the voltage uniformity for dynamic loading of a PEM fuel cell stack, Int. J. Hydrogen Energy. 40 (2015) 7361–7369. https://doi.org/10.1016/j.ijhydene.2015.04.058.

[27] J.A. Salva, A. Iranzo, F. Rosa, E. Tapia, E. Lopez, F. Isorna, Optimization of a PEM fuel cell operating conditions: Obtaining the maximum performance polarization curve, Int. J. Hydrogen Energy. 41 (2016) 19713–19723. https://doi.org/10.1016/j.ijhydene.2016.03.136.

[28] H. Heidary, M. Jafar Kermani, N. Khajeh-Hosseini-Dalasm, Performance analysis of PEM fuel cells cathode catalyst layer at various operating conditions, Int. J. Hydrogen Energy. 41 (2016) 22274–22284. https://doi.org/10.1016/j.ijhydene.2016.08.178.

[29] P. Pei, X. Yuan, J. Gou, P. Liiam, Dynamic response during PEM fuel cell loading-up, Materials

(Basel). 2 (2009) 734–748. https://doi.org/10.3390/ma2030734.

[30] J. Li, H. Pan, S.J. Zhang, L.F. Sun, Development of the On-Line Monitoring System for Fuel Cell Voltage, Adv. Mater. Res. 219–220 (2011) 383–386. https://doi.org/10.4028/www.scientific.net/AMR.219-220.383.

[31] P. Liu, S. Xu, J. Fu, C. Liu, Experimental investigation on the voltage uniformity for a PEMFC stack with different dynamic loading strategies, Int. J. Hydrogen Energy. 45 (2020) 26490–26500. https://doi.org/10.1016/j.ijhydene.2020.05.070.

[32] M. Mohsin, R. Raza, M. Mohsin-ul-Mulk, A. Yousaf, V. Hacker, Electrochemical characterization of polymer electrolyte membrane fuel cells and polarization curve analysis, Int. J. Hydrogen Energy. 45 (2020) 24093–24107. https://doi.org/10.1016/j.ijhydene.2019.08.246.

[33] T. Wilberforce, A.G. Olabi, Proton exchange membrane fuel cell performance prediction using artificial neural network, Int. J. Hydrogen Energy. 46 (2021) 6037–6050. https://doi.org/10.1016/j.ijhydene.2020.07.263.

[34] A. Abbas, S. Abbas, A. Bhattarai, N.M. Latiff, N. Wai, A.N. Phan, T.M. Lim, Effect of electrode porosity on the charge transfer in vanadium redox flow battery, J. Power Sources. 488 (2021) 229411. https://doi.org/10.1016/j.jpowsour.2020.229411.

[35] L. Jin, X.J. Wang, J.W. Zhu, C.F. Wang, T.T. Zhou, X.W. Zhang, Sensitivity analysis of proton exchange membrane fuel cell performance to operating parameters and its applicability assessment under different conditions, Energy Convers. Manag. 228 (2021) 113727. https://doi.org/10.1016/j.enconman.2020.113727.

[36] S.M. Rezaei Niya, M. Hoorfar, Study of proton exchange membrane fuel cells using electrochemical impedance spectroscopy technique – A review, J. Power Sources. 240 (2013) 281–293.

https://doi.org/10.1016/j.jpowsour.2013.04.011.

[37] H. Yuan, H. Dai, X. Wei, P. Ming, Internal polarization process revelation of electrochemical impedance spectroscopy of proton exchange membrane fuel cell by an impedance dimension model and distribution of relaxation times, Chem. Eng. J. 418 (2021) 129358. https://doi.org/10.1016/j.cej.2021.129358.

[38] M. Heinzmann, A. Weber, E. Ivers-Tiffée, Advanced impedance study of polymer electrolyte membrane single cells by means of distribution of relaxation times, J. Power Sources. 402 (2018) 24–33. https://doi.org/10.1016/j.jpowsour.2018.09.004.

[39] J. Jung, Y.H. Chung, H.Y. Park, J. Han, H.J. Kim, D. Henkensmeier, S.J. Yoo, J.Y. Kim, S.Y. Lee, K.H. Song, H.S. Park, J.H. Jang, Electrochemical impedance analysis with transmission line model for accelerated carbon corrosion in polymer electrolyte membrane fuel cells, Int. J. Hydrogen Energy. 43 (2018) 15457–15465. https://doi.org/10.1016/j.ijhydene.2018.06.093.

[40] Z. Tang, Q.-A. Huang, Y.-J. Wang, F. Zhang, W. Li, A. Li, L. Zhang, J. Zhang, Recent progress in the use of electrochemical impedance spectroscopy for the measurement, monitoring, diagnosis and optimization of proton exchange membrane fuel cell performance, J. Power Sources. 468 (2020) 228361. https://doi.org/10.1016/j.jpowsour.2020.228361.

[41] M. Voigts, A. Kru, H. Schichlein, A.C. Mu, A.C. Müller, M. Voigts, A. Krügel, E. Ivers-Tiffée, Deconvolution of electrochemical impedance spectra for the identification of electrode reaction mechanisms in solid oxide fuel cells, J. Appl. Electrochem. 32 (2002) 875–882. https://doi.org/10.1023/A:1020599525160.

[42] S. Simon Araya, F. Zhou, S. Lennart Sahlin, S. Thomas, C. Jeppesen, S. Knudsen Kær, Fault Characterization of a Proton Exchange Membrane Fuel Cell Stack, Energies. 12 (2019) 152.

https://doi.org/10.3390/en12010152.

[43] D. Klotz, J.P. Schmidt, A. Kromp, A. Weber, E. Ivers-Tiffée, The Distribution of Relaxation Times as Beneficial Tool for Equivalent Circuit Modeling of Fuel Cells and Batteries, ECS Trans. 41 (2019) 25–33. https://doi.org/10.1149/1.3692958.

[44] Y. Aoyama, K. Suzuki, Y. Tabe, T. Chikahisa, Observation of water transport in the micro-porous layer of a polymer electrolyte fuel cell with a freezing method and cryo-scanning electron microscope, Electrochem. Commun. 41 (2014) 72–75. https://doi.org/10.1016/j.elecom.2013.12.029.

[45] P. Deevanhxay, T. Sasabe, K. Minami, S. Tsushima, S. Hirai, Oblique Soft X-Ray Tomography as a Non-Destructive Method for Morphology Diagnostics in Degradation of Proton-Exchange Membrane Fuel Cell, Electrochim. Acta. 135 (2014) 68–76. https://doi.org/10.1016/j.electacta.2014.04.144.

[46] G. Wang, F. Huang, Y. Yu, S. Wen, Z. Tu, Degradation behavior of a proton exchange membrane fuel cell stack under dynamic cycles between idling and rated condition, Int. J. Hydrogen Energy. 43 (2018) 4471–4481. https://doi.org/10.1016/j.ijhydene.2018.01.020.

[47] J. Farmer, B. Duong, S. Seraphin, S. Shimpalee, M.J. Martínez-Rodríguez, J.W. Van Zee, Assessing porosity of proton exchange membrane fuel cell gas diffusion layers by scanning electron microscope image analysis, J. Power Sources. 197 (2012) 1–11. https://doi.org/10.1016/j.jpowsour.2011.08.064.

[48] T. Lochner, L. Hallitzky, M. Perchthaler, M. Obermaier, J. Sabawa, S. Enz, A.S. Bandarenka, Local degradation effects in automotive size membrane electrode assemblies under realistic operating conditions, Appl. Energy. 260 (2020) 114291. https://doi.org/10.1016/j.apenergy.2019.114291.

[49] B.A. Boukamp, A Linear Kronig- Kramers Transform Test for Immittance Data Validation, J.

Electrochem. Soc. 142 (1995) 1885–1894. https://doi.org/10.1149/1.2044210.

[50] M. Schönleber, D. Klotz, E. Ivers-Tiffée, A Method for Improving the Robustness of linear Kramers-Kronig Validity Tests, Electrochim. Acta. 131 (2014) 20–27. https://doi.org/10.1016/j.electacta.2014.01.034.

[51] M. Schönleber, Kramers-Kronig Validity Test Lin-KK for Impedance Spectra, (n.d.), https://www.iam.kit.edu/wet/english/Lin-KK.php.

[52] A.N. Tikhonov, A. V. Goncharsky, V. V. Stepanov, A.G. Yagola, Numerical Methods for the Solution of Ill-Posed Problems, 1995. https://doi.org/10.1007/978-94-015-8480-7.

[53] S.K. Roy, M.E. Orazem, B. Tribollet, Interpretation of Low-Frequency Inductive Loops in PEM Fuel Cells, J. Electrochem. Soc. 154 (2007) B1378. https://doi.org/10.1149/1.2789377.

Graphical Abstract

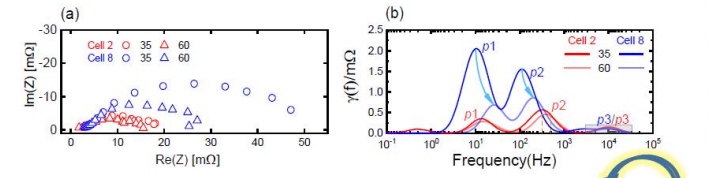

Impedance-based analysis for cell inconsistency

Validation

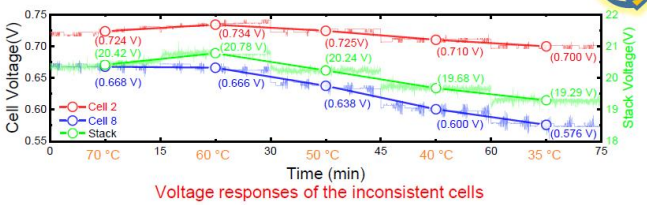

Voltage responses of the inconsistent cells

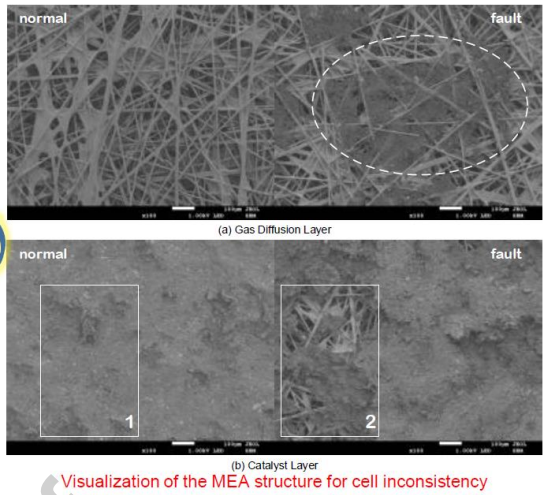

Visualization of the MEA structure for cell inconsistency